

Machine-Learning-Assisted and Real-Time-Feedback-Controlled Growth of InAs/GaAs Quantum Dots

Chao Shen,^{†,§} Wenkang Zhan,^{†,‡} Kaiyao Xin,^{‡,§} Manyang Li,^{†,‡} Zhenyu Sun,^{†,‡} Jian Tang,^{||} Zhaofeng Wu,[§] Bo Xu,^{†,‡} Zhongming Wei,^{‡,§} Chao Zhao,^{*,†,‡} and Zhanguo Wang^{†,‡}

[†] Key Laboratory of Semiconductor Materials Science, Institute of Semiconductors, Chinese Academy of Sciences & Beijing Key Laboratory of Low Dimensional Semiconductor Materials and Devices, Beijing 100083, China

[‡] College of Materials Science and Opto-Electronic Technology, University of Chinese Academy of Science, Beijing 101804, China

[#] State Key Laboratory of Superlattices and Microstructures, Institute of Semiconductors, Chinese Academy of Sciences, Beijing 100083, China

[§]School of Physics Science and Technology, Xinjiang University, Urumqi, Xinjiang 830046, China

^{||} School of Physical and Electronic Engineering, Yancheng Teachers University, Yancheng 224002, China

*Email: zhaochao@semi.ac.cn

ABSTRACT

Self-assembled InAs/GaAs quantum dots (QDs) have properties highly valuable for developing various optoelectronic devices such as QD lasers and single photon sources. The applications strongly rely on the density and quality of these dots, which has motivated studies of the growth process control to realize high-quality epi-wafers and devices. Establishing the process parameters in molecular beam epitaxy (MBE) for a specific density of QDs is a multidimensional optimization challenge, usually addressed through time-consuming and iterative trial-and-error. Meanwhile, reflective high-energy electron diffraction (RHEED) has been widely used to capture a wealth of growth information *in situ*. However, it still faces the challenges of extracting information from noisy and overlapping images. Here, based on 3D ResNet, we developed a machine learning (ML) model specially designed for training RHEED videos instead of static images and providing real-time feedback on surface morphologies for process control. We demonstrated that ML from previous growth could predict the post-growth density of QDs, by successfully tuning the QD densities in near-real time from $1.5 \times 10^{10} \text{ cm}^{-2}$ down to $3.8 \times 10^8 \text{ cm}^{-2}$ or up to $1.4 \times 10^{11} \text{ cm}^{-2}$. Compared to traditional methods, our approach, with *in-situ* tuning capabilities and excellent reliability, can dramatically expedite the material optimization process and improve the reproducibility of MBE growth, constituting significant progress for thin film growth techniques. The concepts and methodologies proved feasible in this work are promising to be applied to a variety of material growth processes, which will revolutionize semiconductor manufacturing for microelectronic and optoelectronic industries.

KEYWORDS: Molecular Beam Epitaxy, Quantum dots, Machine Learning, Reflective high-energy electron diffraction, Real-time Control

Self-assembled quantum dots (QDs) have attracted great interest due to their applications in various optoelectronic devices.¹ The so-called Stranski-Krastanow (SK) mode in molecular beam epitaxy (MBE) is widely used for growing these high-quality QDs.² For specific applications, such as QD lasers, high QD densities are required; while low-density QDs are necessary for other applications, such as single photon sources.¹ However, the outcomes of any QD growth process are a complex function of a large number of variables including the substrate temperature, III/V ratio, and growth rate, etc. Building a comprehensive analytical model that describes complex physical processes occurring during growth is an intractable problem.³ The optimization of material growth largely depends on the skills and experience of MBE researchers. Time-consuming trial-and-error testing is inevitably required to establish optimal process parameters for the intended material specification.

Machine learning (ML) is revolutionary due to its exceptional capability for pattern recognition and establishing complex systems' empirical functions. It enables researchers to extract valuable insights and identify hidden patterns from large datasets, leading to a better understanding of complex phenomena required to build predictive models, generate new hypotheses, and determine optimal growth conditions for MBE.⁴⁻⁷ However, these remain *posteriori* ML-based approaches, since they require the completion of the entire growth run. Therefore, once the sample characterization results deviate, it becomes challenging and time-consuming to identify reasons.⁸ In contrast, by enabling the direct adjustment of parameters during material growth, ML-based *in-situ* control can detect and correct any deviation from expected values in a timely manner.⁸⁻¹⁰ Meng et al. have utilized a feedback control to adjust cell temperatures during growth, thereby capable of regulating $\text{Al}_x\text{Ga}_{1-x}\text{As}$ compositions *in situ*.¹⁰ It offers an alternative approach where the growth

outcomes for an arbitrary set of parameters can be accurately predicted via a trained neural network, which has been applied to extract film thickness and growth rate information.^{11, 12}

Before controlling parameters during the MBE growth, obtaining accurate information on the current material status is a prerequisite. Reflection high-energy electron diffraction (RHEED) is crucial as an in-situ characterization tool for material growth.¹³ Traditionally, identifying RHEED patterns during material growth was mainly depended on the experience of growers. Progress has been made in the automatic classification of RHEED patterns through ML that incorporates principal component analysis (PCA) and clustering algorithms.^{11, 13-16} It surpasses human analysis when a single static RHEED image is gathered with the substrate held at a fixed angle.^{15, 17} However, this may result in an incomplete utilization of the temporal information available in RHEED videos taken with the substrate rotating continuously.^{15, 18, 19} Although few scholars have highlighted the importance of analyzing RHEED videos, their ML models were still based on PCA and encoder-decoder architecture with a single image input.^{15, 20}

In this work, we have developed an in-situ characterization and real-time control method based on ML to optimize the material growth. We investigated the temporal evolving of RHEED information during the growth of InAs QDs on GaAs substrates. The existing RHEED videos of the QD growth process is segmented and used as an ML sample for model training. Based on the density of QDs measured by atomic force microscopy (AFM), the RHEED video sequences were classified into four categories. We applied two structurally identical 3D ResNet 50 models, which takes three-dimensional variables as inputs to classify density and determine the QD formation.²¹ We showed that ML can simulate and predict the post-growth material specifications, and based on which, growth parameters are continuously monitored and adjusted. Our results demonstrated that the QD densities were successfully tuned from $1.5 \times 10^{10} \text{ cm}^{-2}$ down to $3.8 \times 10^8 \text{ cm}^{-2}$, and up

to $1.4 \times 10^{11} \text{ cm}^{-2}$, respectively. The effectiveness of our approach by taking full advantages of in situ characterization marked a significant achievement of establishing a precise growth control scheme, with the capabilities and potentials of being extended to large-scale material growth, reducing the impact on material growth due to instability and uncertainty of MBE operation, shortening the parameter optimization cycle, and improving the final yield of material growth.

Results and Discussion

Sample structure and data labeling

Our method relied on an existing database of growth parameters with corresponding QD characteristics, which helped us decide the growth parameters needed later to achieve a target density value for QDs. The density results of QDs were summarized in Figure 1b, which was correlated with the RHEED video. The samples grown without QDs have flat surfaces, corresponding to streaky RHEED patterns, as shown in Figures 1c and 1g, which was artificially labeled with “zero”.²² With the increase of QD density, it was found that the RHEED gradually converted from streaky to spot patterns. The “low” density range was defined at which the RHEED pattern consisted of streak and spot.²² As shown in Figures 1d and 1h, the density of QDs was approximately $1.7 \times 10^9 \text{ cm}^{-2}$. As shown in Figure 1e and 1i, with the further increase of QD density reaching $2.9 \times 10^{10} \text{ cm}^{-2}$, the arrangement of spots in the RHEED pattern showed typical spot-like features.²³⁻²⁵ By further analyzing the RHEED pattern, we found that the transition from features with both streaks and spots to those only with spots typically occurred at a QD density of $1 \times 10^{10} \text{ cm}^{-2}$. Therefore, we assigned the label “middle” to the densities exceeding $1 \times 10^{10} \text{ cm}^{-2}$. To carefully evaluate the evolving of increasing QDs density, we collected more data sets within the density range from $1 \times 10^{10} \text{ cm}^{-2}$ to $4 \times 10^{10} \text{ cm}^{-2}$. Finally, we assigned the label “high” to those

with densities above $4 \times 10^{10} \text{ cm}^{-2}$ (see the Supporting Information for RHEED characteristics of QDs with different labels, S1). Figures 1f and 1j show the typical AFM and RHEED after the QD formation, respectively, with the QD density of approximately $6.5 \times 10^{10} \text{ cm}^{-2}$ in the AFM image. It is worth noting that we keep the labels to the RHEED videos the same before and after the QD formation. The RHEED information before the QD formation can be used to determine the resulting QD density grown under the current conditions, enabling us to adjust the material growth parameters before the QD formation.

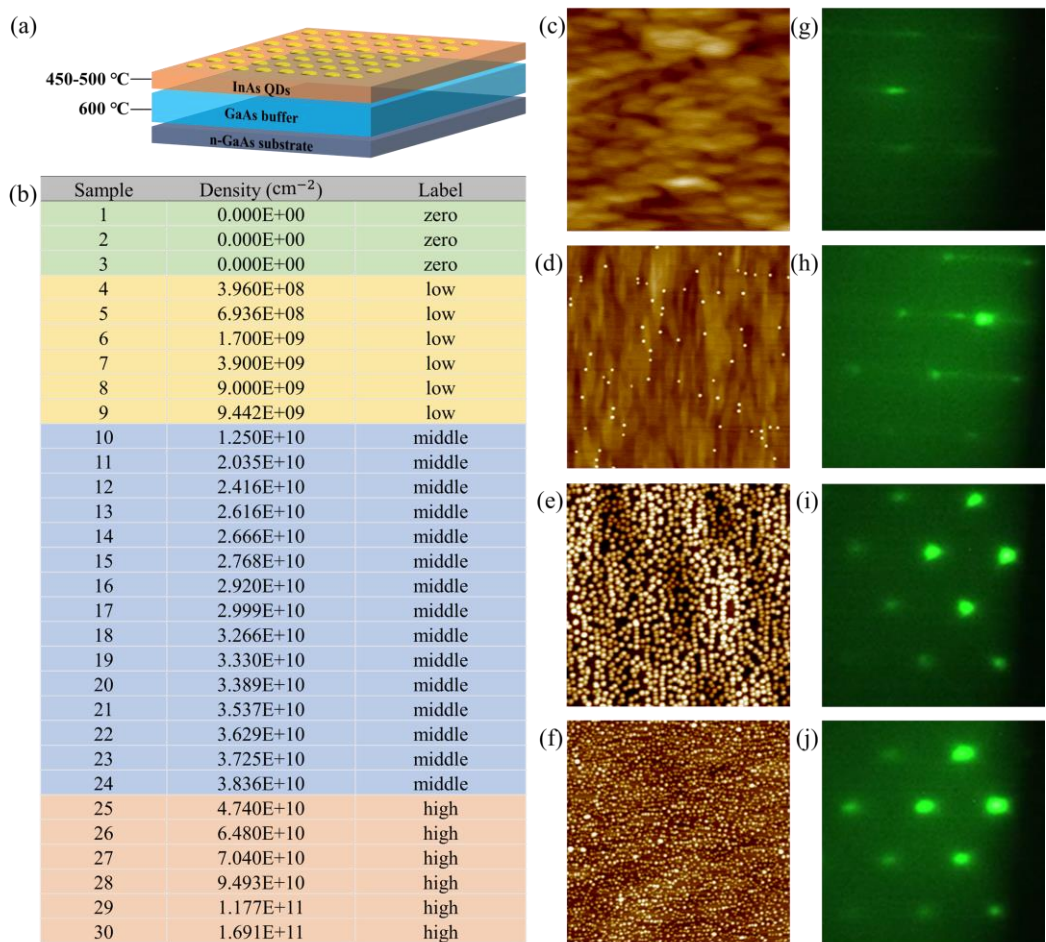


Figure 1. (a) The schematic of the sample structure. (b) QD densities and labels assigned for the samples in the dataset, the density of QDs was determined by counting the number of QDs visibly

in the AFM image. (c-f) The $2 \mu\text{m} \times 2 \mu\text{m}$ AFM images of QDs with varied labels. (g-j) Corresponding RHEED images of QDs with varied labels.

Program framework and video processing

The design framework of the program is illustrated in Figure 2a (see the Supporting Information for hardware wiring schematic for model deployment and program interface and deployment environment, S2 and S3). An appropriate scheme was designed to pre-process the RHEED video data. Then, a ML model was selected based on the pre-processing results. In addition, we also determined the way to adjust parameters according to output results of the model.

The images collected were uncompressed 4 channels of 8-bit depth color images with a resolution of 1920×1200 , as shown in Figure 2b. The software cropped a square area from the image, immediately compressed to 300×300 by zero-order sampling and converted it to a single $4 \times 300 \times 300$ matrix, as shown in Figure 2c (see the Supporting Information for the cropping area for RHEED images, S4). To efficiently utilize the temporal information within RHEED data, we used the latest RHEED image as a starting point, acquired an additional seven consecutive images before, and bundled as the original RHEED dataset for the model, as shown in Figure 2d.²⁶ Subsequently, each image was converted to a single-channel 8-bit grayscale image based on the luminance information,^{15, 20} and stitched into an $8 \times 300 \times 300$ 3D matrix through shift registers, as shown in Figure 2e. Additionally, we modified the convolutional filtering order. Traditional convolutional neural networks (CNNs) tend to uniformly sample color channels, which is effective for images with rich color information,^{27, 28} which is not suitable for our data. To address this issue, we designed a novel image processing approach that uses longitudinal size information instead of color channel information, which can improve the correlation between channels, reduce

unnecessary calculations, and improve data processing efficiency.²⁹⁻³¹ Therefore, the size of the preprocessed data was $8 \times 300 \times 1 \times 300$, representing the image number, image width, image color channel, and image length.

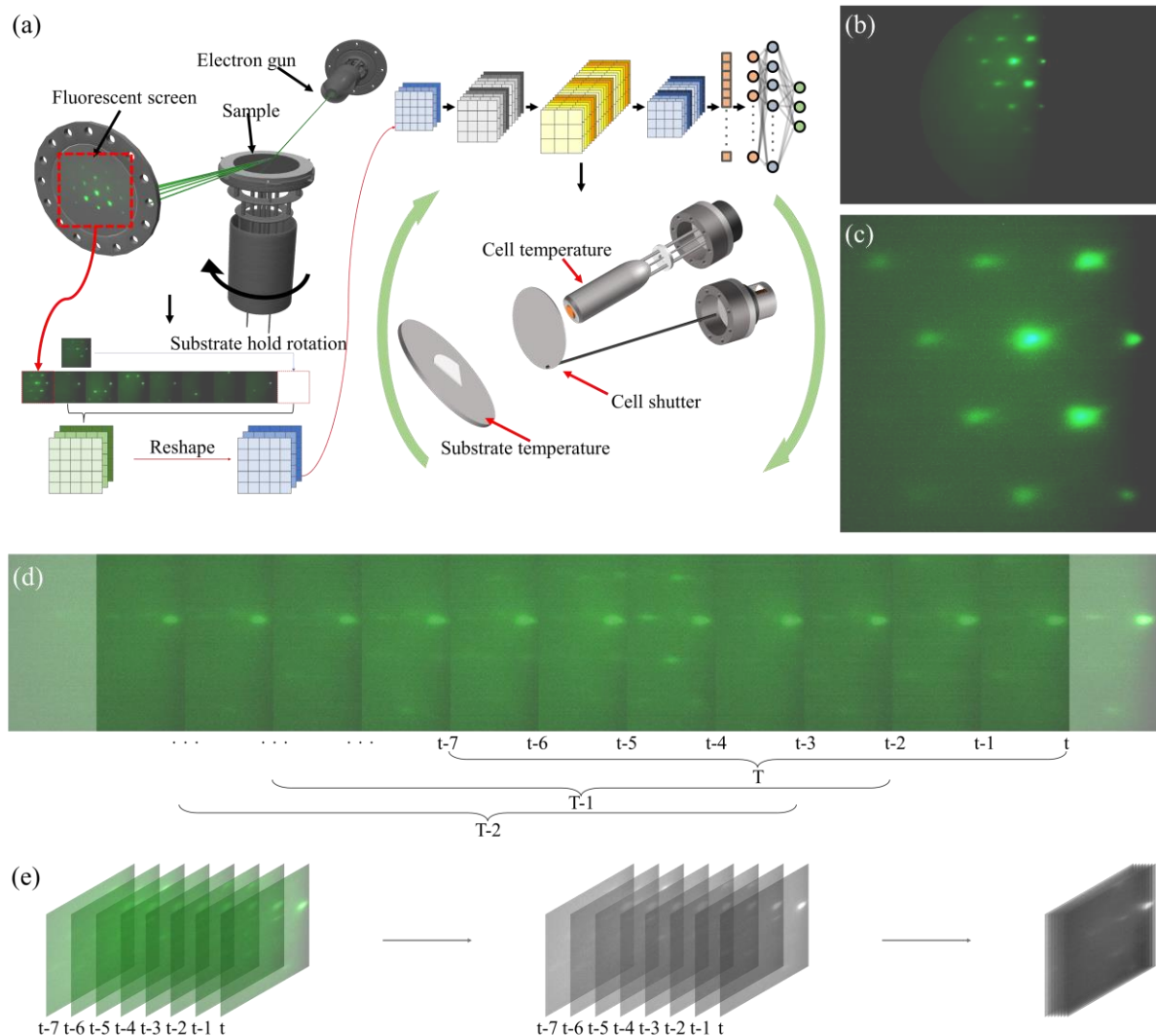


Figure 2. (a) The framework of the program. (b) A typical original RHEED image taken from the camera. (c) The image after cropping. (d) Continuous sampling method for RHEED images. (e) Processing method for sampled images.

Model construction and evaluation

The basic residual blocks of the 3D ResNet 50 model we used are Residual Block 1 and Residual Block 2, as shown in Figures 3a and 3b, respectively. Figure 3a illustrates two pathways for data processing, one utilizing identity shortcuts and the other combining two sets of 3D convolutional layers with 3D batch normalization, connected via the ReLU activation function. Identity shortcuts eliminate computing convolutional layers and batch normalization, resulting in no additional overhead on training speed and model size without compromising model performance.^{32, 33} Figure 3b depicts a residual structure formed by replacing the path utilizing identity shortcuts in Figure 3a with 3D convolutional kernels and 3D batch normalization. These basic residual blocks not only promptly drop unfavorable training parameters thereby efficiently train deep neural networks, but also learn temporal and spatial relationships within video data simultaneously.³⁴⁻³⁶ Based on two basic residual blocks, the other residual structures in the model were composed, namely, Basic Block 1, Basic Block 2, Basic Block 3, and Basic Block 4, respectively. Each residual block is constructed by stacking multiple convolution layers and basic residual blocks. Before these residual structures are connected, there is also a Basic Stem, as shown in Figure 3c. This spatiotemporal-feature-learning method enables the 3D ResNet 50 model better capture the dynamic information in videos compared to 2D CNN, resulting in an enhanced ability to identify and differentiate the categories of videos.^{37, 38}

The structures of Basic Stem and each residual structure are shown in Figures 3d-3h. In the Basic Stem, the data dimensions are expanded from 8 to 64 using basic 3D convolution layers, as shown in Figure 3d. In Basic Block 1, the first residual calculation is performed using an identity mapping to construct an identity residual block, as shown in Figure 3e.³⁹ As data is processed in Basic Block 2 and Basic Block 3 as shown in Figures 3f and 3g, projection shortcut are added during residual

calculation to construct convolutional residual blocks, allowing the data to expand from 64 to 128 and 256 dimensions.⁴⁰⁻⁴³ In this way, the network can effectively maintain the information flow and avoid the risk of gradient vanishing.⁴⁴ In Basic Block 4, the data pass through the basic residual block and ReLu activation function multiple times, and undergo processing through an average pooling layer, a flatten layer, and a fully connected layer for producing the final classification results, as shown in Figure 3h.

We trained models for classifying density and judging the QDs formation, which are called the “density model” and the “QDs model”, respectively. The accuracy and loss of each model during the training are shown in Figures 3i and 3j. Overall, the improvement trend of accuracy for the two models is evident. However, the validation accuracy of the “density model” fluctuates considerably even after 100 epochs, as shown in Figure 3i. After 120 training epochs, the “QDs model” maintains an average validation accuracy of over 90%, although its validation accuracy also fluctuated as shown in Figure 3j. This is primarily due to certain RHEED features appeared in multiple labels. To address this issue, we have utilized multiple consecutive discriminant results obtained from the model. The probability of occurrence is then calculated for each result. The result with the highest probability is selected to determine whether the adjustment to the growth parameters is necessary.

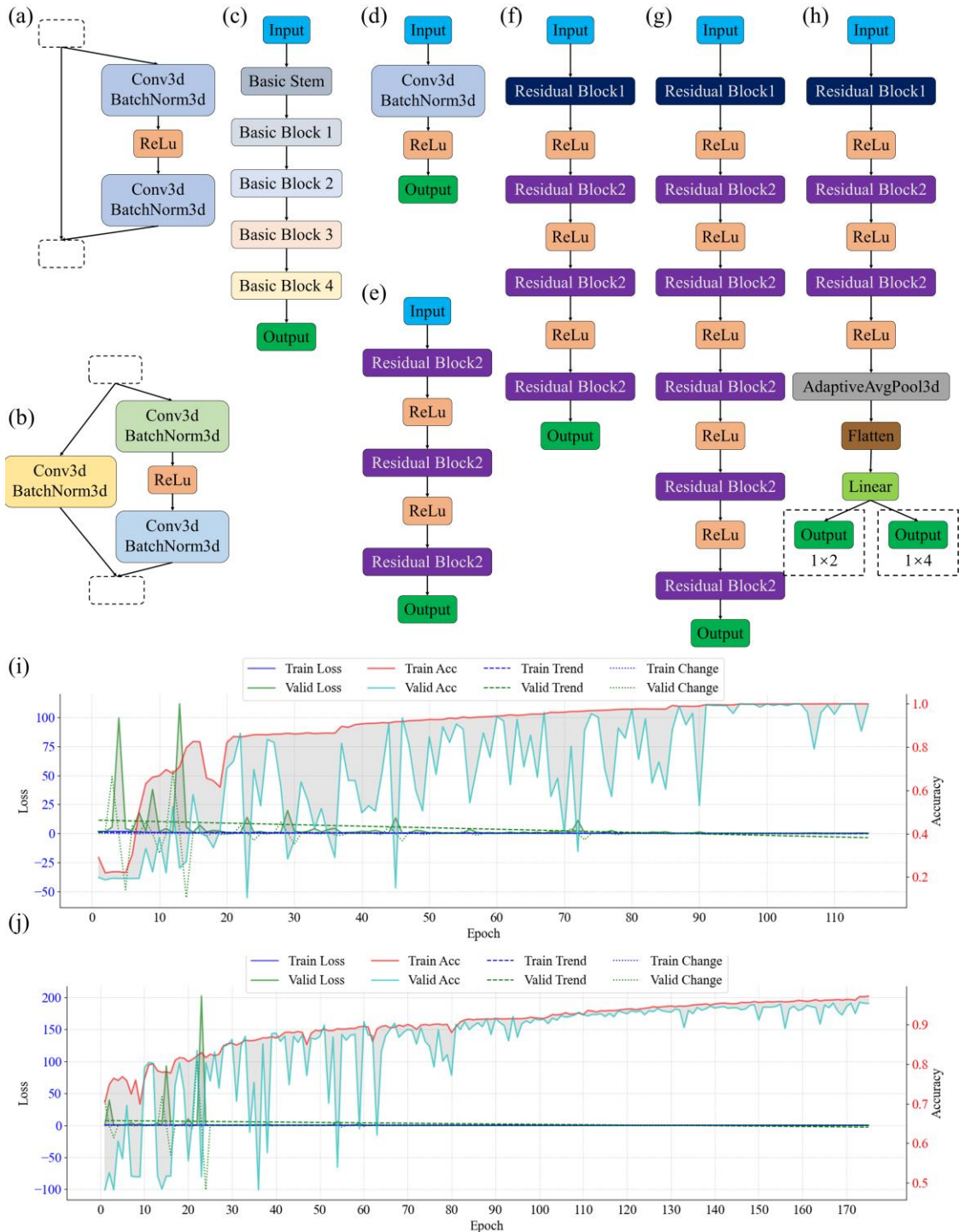


Figure 3. Structure diagrams of (a) Residual Block 1, (b) Residual Block 2, (c) 3D ResNet 50 Model, (d) Basic Stem, (e) Basic Block 1, (f) Basic Block 2, (g) Basic Block 3, and (h) Basic Block

4. Training performance of (i) “density model”, and (j) “QDs model”: accuracy and loss as a function of trend variation.

Controlled growth of low-density QDs

We have also grown a reference sample with QD density of $1.5 \times 10^{10} \text{ cm}^{-2}$, corresponding to label “middle” (see the Supporting Information for details of the reference sample, S5). Subsequently, we set the initial substrate temperature equivalent to that used in the reference sample and conducted in-situ control experiment with the “low” or “high” label as the target (see the Supporting Information for videos for the experiments). After growth, we compiled each frame of the RHEED image captured during the growth into a sequence and analyzed. In order to distinguish the different growth stages of the material under model control, we marked the QD formation time and the In shutter closing time judged by the model in the sequence, with blue and yellow lines in the Figures 4 and 5.

As shown in Figure 4a, the substrate temperature increased by 44 °C from the beginning of the sequence until the In shutter was closed. This indicates that the initial substrate temperature was not suitable for the “low” label. In addition, the blue line and yellow line are in the same sequence, indicating that when the QDs are formed, the “density model” has already determined that the current RHEED sequences are consistent with the “low” label. As shown in Figure 4b, the RHEED images mainly presents streak in the initial growth stage of QDs; it kept even before the QD formation, as shown in Figure 4c. This is attributed to the relatively flat surface of the material in the early stage of QD growth. After the QD formation, a pattern coexisting streaks and spots was immediately observed as shown in Figure 4d, consistent with the “low” label characteristics.²² The QDs has a density of $3.8 \times 10^8 \text{ cm}^{-2}$, with an average diameter of 50.5 nm and height of 10.0 nm,

as shown in the AFM image in Figure 4e. The result confirms the accuracy of the “density model” prediction in achieve a QD density labeled as “low”.

Figure 4f shows the output for the “QDs model” during entire sequences. We also performed probability statistics on model results. Before the QD formation, the model primarily output “No”. However, after the blue line, we observed a significant increase in the probability of output “Yes”, indicating the model has a sensitivity in determining the formation of low density QDs (see the Supporting Information for the statistical analysis of the “density model”, S6).

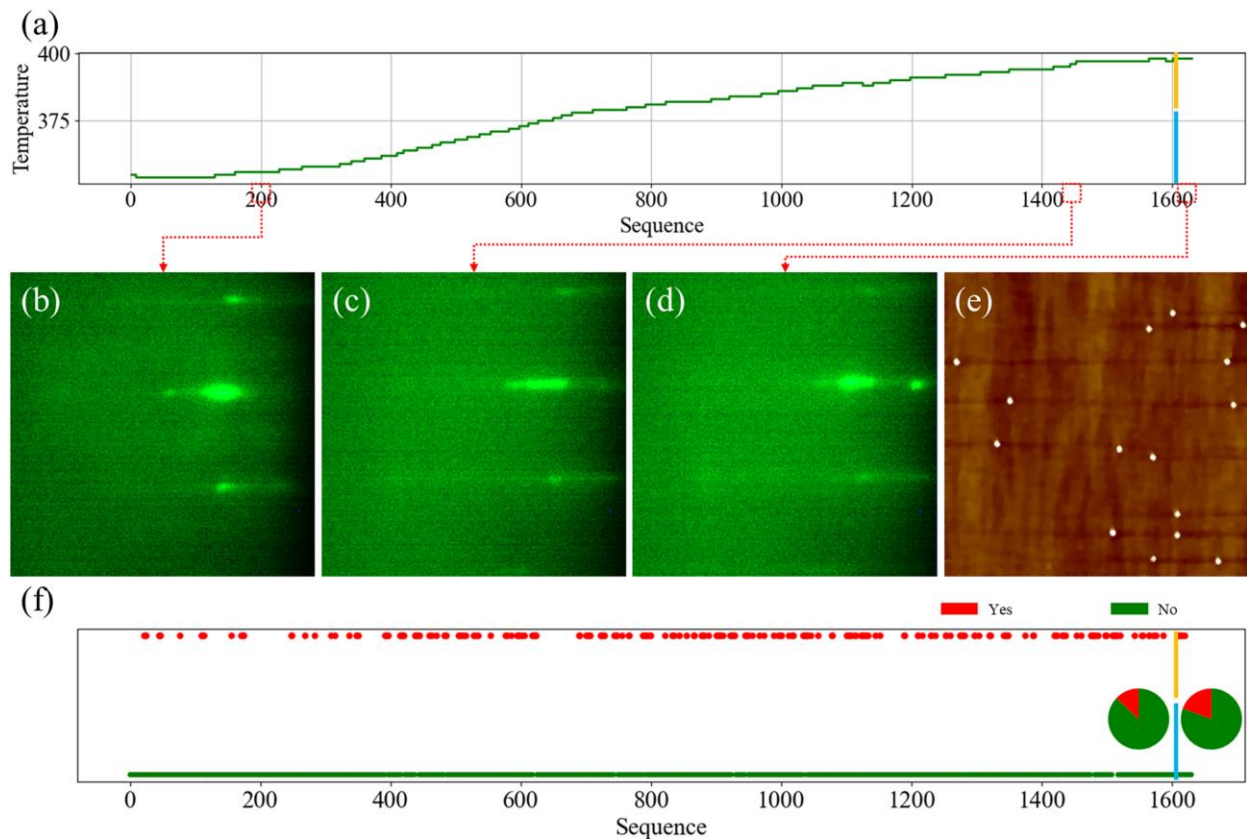


Figure 4. Experiment with the “low” label as the target, blue line: the QD formation time; yellow line: the In shutter closing time. (a) Substrate temperature changes during growth. The RHEED image (b) captured at 200th frame after growth; (c) before the QD formation; (d) after the QD formation. (e) The $2 \mu\text{m} \times 2 \mu\text{m}$ AFM image of the sample grown with the “low” label as the target. (f) The prediction results of the “QDs model”, pie charts in the inset representing the probability

of the results predicted. We classified RHEED videos as the “Yes” or “No” based on visual observations of whether QDs had been formed or not.

Controlled growth of high-density QDs

We also conducted an in-situ control experiment with the “high” label as the target. From Figure 5a, it can be observed that the substrate temperature decreased by a total of 24 °C, indicating that the initial substrate temperature was not suitable for “high” label. In addition, the blue line in the figure did not overlap with the yellow line, which indicates the RHEED image with “high” label did not appear during the initial stage of the QD formation. In the initial stage of InAs growth, the RHEED pattern still primarily showed streak patterns, as shown in Figure 5b. As the deposition amount increased, the streaks gradually became blurred before the QD formation, indicating that a certain amount of InAs has already deposited on the substrate surface and caused the surface to become rough, as shown in Figure 5c. As shown in Figure 5d, the RHEED pattern showed streaks and spots after the QD formation like those shown in Figure 4d, which are typical features of the “low” label. This explains why the blue line and the yellow line in Figure 5a did not coincide. As the In shutter closed, and the RHEED pattern exhibited spots, as shown in Figure 5e. The QDs density is approximately $1.4 \times 10^{11} \text{ cm}^{-2}$ with an average diameter of 33.5 nm and height of 3.2 nm, as shown in Figure 5f. As shown in Figure 5g, the model almost exclusively output “Yes”, indicating high accuracy in recognizing spots pattern after the QD formation. It is noteworthy that there is still a distance between the blue line and the last “No” label, since we confirm the QD formation by collecting multiple results of the model.

Note our experiment has a certain failure rate due to limited dataset, the accuracy of the model, and data labeling.⁴⁵⁻⁴⁷ In our experiment, each prediction takes a few seconds, which is limited by

the graphics card of our setup; the communication between the server and MBE controller takes seconds which is determined by wiring, the baud rates of serial communication, and the output power of controller. By upgrading the hardware of our MBE system, a few tens of milliseconds of response can be achieved using the same workflow developed in this report.

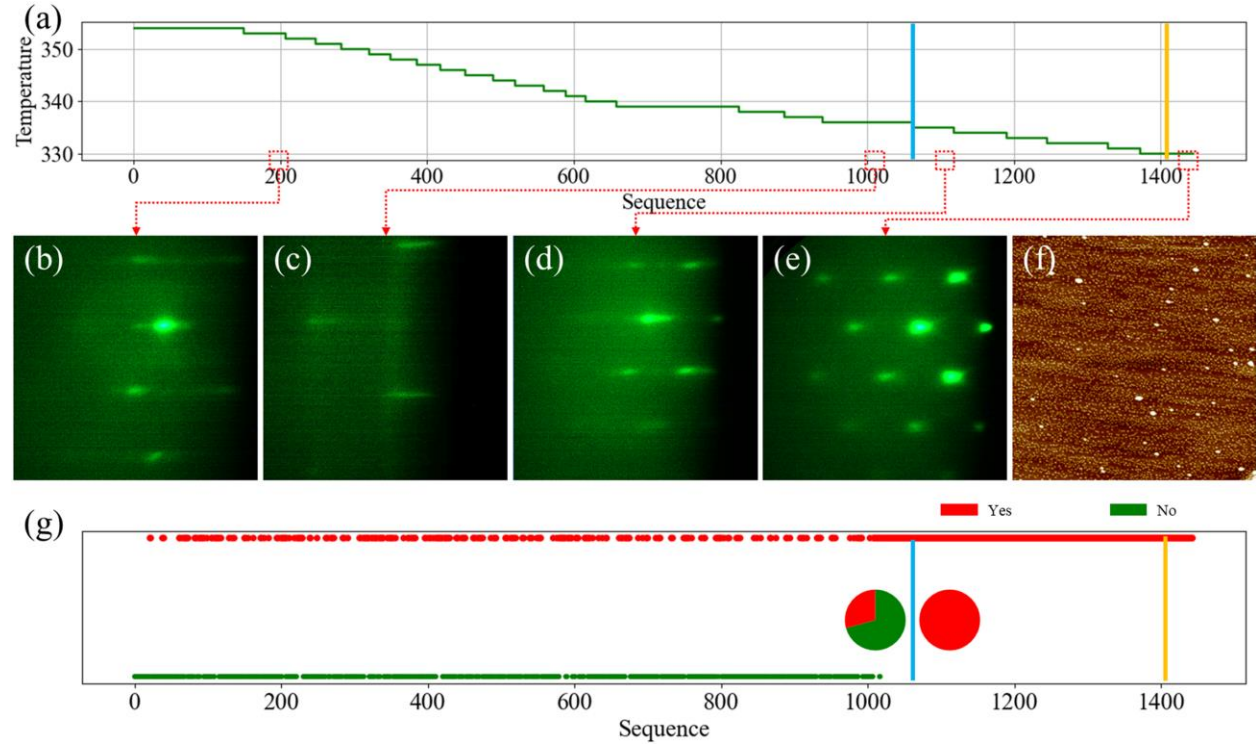


Figure 5. Experiment with the “high” label as the target, blue line: the QD formation time; yellow line: the In shutter closing time. (a) Substrate temperature changes during growth. The RHEED image (b) captured at 200th frame after growth; (c) before the QD formation; (d) after the QD formation; (e) before the end of the growth process. (f) The $2 \mu\text{m} \times 2 \mu\text{m}$ AFM image of the sample grown with the “high” label as the target. (g) The prediction results of the “QDs model”, pie charts in the inset representing the probability of the results predicted.

Conclusions

In conclusion, we developed a metrology to control the material's properties grown by MBE in-situ. We showed that a neural network could accurately predict the post-growth density of QDs within a wide range by utilizing RHEED videos information of as-grown samples. We applied the method to InAs/GaAs QDs by tuning growth parameters in near real-time and validated it to in-situ control the QD density, which is usually only possible by trial-and-error. The capability can significantly reduce the time and the number of experimental iterations required for development and optimization to achieve material specifications. In this proof-of-concept study, we trained a network to simulate a specific type of MBE growth task by varying the substrate temperature. In practice, one would train the network to the tasks with a full range of system metadata. In this way, the network would accrue an “understanding” of the complex relationships among the numerous sample and system parameters that affect the growth outcomes. Our investigations highlighted the considerable strength and practicality of the growth metrology to achieve high-quality epitaxial thin films for various applications. Moving forward, there is a huge potential for such networks to be deployed for defect detection, identification, and repair during material growth at an early stage.

Experimental Section

Material growth

The InAs QD samples were grown on GaAs substrates in the Riber 32P MBE system, equipped with arsenic (As) valved cracker, indium (In), and gallium (Ga) effusion cells. As₄ was used in the growth by keeping the cracker temperature at 600 °C. The beam equivalent pressure (BEP) was used to evaluate the flux of the III and V elements and calibrate their ratio.⁴⁸ A C-type thermocouple measured the substrate temperature, and the growth rates were calibrated through the RHEED oscillations of extra layers grown on GaAs substrates. The substrate was outgassed at

350 °C in the buffer chamber, then heated to 620 °C in the growth chamber for deoxidation. The substrate was then cooled to 600 °C for the growth of the GaAs buffer layer subsequently. The sample structure is shown in Figure 1a. The BEP of In was $1.4 \sim 1.5 \times 10^{-8}$ Torr, while the BEP of As was $0.95 \sim 1.0 \times 10^{-7}$ Torr. The QDs were formed in the SK growth mode after depositing 1.7 ML of InAs at a temperature of 450 ~ 500 °C and a rate of 0.01 ML/s. The initial growth showed a relatively flat planar structure, pertaining to the wetting layer growth.⁴⁹⁻⁵⁴ The formation of InAs QDs was verified by the streaky-spotty transition.⁵⁵

Material characterization

RHEED in the MBE growth chamber enabled us to analyze and monitor the surface of the epilayer during the growth. RHEED patterns were recorded at an electron energy of 12 kV (RHEED 12, from STAIB). A darkroom equipped with a camera was placed outside the chamber to continuously collect RHEED images with the substrate rotating at 20 rpm. The exposure time was 100 ms, with a frame sampling rate of 8 frames per second. To achieve a clear correlation of RHEED with QD density, we also characterized the surface morphology of the InAs QDs using AFM (Dimension Icon, from Burker).

Hardware wiring scheme

The program primarily obtains information from the temperature controllers, shutter controller, and the camera to control temperature and shutter (Figure S4). Temperature controllers are connected in series using the Modbus protocol to simplify the wiring. In order to reduce the delay in substrate temperature control, our program solely looks up information by address from the temperature controllers connected to the substrate.

The principle of the basic residual block in ResNet

The basic residual block of ResNet could be generally given by:⁵⁶

$$y_l = h(x_l) + F(x_l, W_l) \quad (1)$$

$$x_{l+1} = f(y_l) \quad (2)$$

Where x_l and x_{l+1} represent the input and output of the l block, please note that each block typically contains a multi-layer structure. W_l is a set of weights associated with the l residual unit, and could be generally given by:

$$\mathcal{W}_l = \left\{ W_{l,k} \mid_{1 \leq k \leq K} \right\} \quad (3)$$

K in Eqn. (3) is the number of layers in the block. The F is a residual function that represents the learned residual. If we set the function h as an identity mapping, then $h(x_l) = x_l$. The f represent the activation function. Since ReLu activation function only contains a nonlinear threshold, it can effectively solve the problem of gradient disappearance and improve the model's generalization ability. Therefore, we also select ReLu as activation function. If f is also an identity mapping, that is $x_{l+1} \equiv y_l$, we can substitute Eqn. (2) into Eqn. (1) and obtain:

$$x_{l+1} = x_l + F(x_l, W_l) \quad (4)$$

Based on the Eqn. (4), we employed an accumulation method to obtain learned features from the shallow l layer to the deep L layers, as follows:

$$x_L = x_l + \sum_{i=l}^{L-1} F(x_i, W_i) \quad (5)$$

Eqn. (5) exhibits an excellent property: The feature x_L of any deeper unit L can be expressed as the sum of a shallower unit l and a residual function F . This indicates that the model follows a residual fashion between any units L and l . Additionally, from the chain rule of backpropagation, the gradients of the reverse process can be obtained:⁵⁷

$$\frac{\partial \text{loss}}{\partial x_l} = \frac{\partial \text{loss}}{\partial x_L} \cdot \frac{\partial x_L}{\partial x_l} = \frac{\partial \text{loss}}{\partial x_L} \cdot \left(1 + \frac{\partial}{\partial x_l} \sum_{i=l}^{L-1} F(x_i, W_i) \right) \quad (6)$$

The model divides the parameters into two additive terms: items that are passed through weight layers, and items that are not. The first factor of the formula $\frac{\partial \text{loss}}{\partial x_L}$ represents the gradient reached by the loss function at L , and ensures that information is propagated directly back to any shallower unit l . This design scheme allows any unit to be transmitted forward or backward to another unit and ensures that the model does not lose data during information transfer.

Program interface and deployment environment

The program was developed using LabVIEW, the built-in NI VISA, NI VISION, and Python libraries for data acquisition and processing. Figure S5a shows the program interface and the deployment environment. The program also employs ONNX for model deployment and TensorRT for inference acceleration. As shown in Figure S5b, this program allows users to set targets for the desired QD density. Once the substrate and In cell temperatures have stabilized, the program can be initiated. Firstly, the program checks the shutter status and controls the substrate and cell temperature. Once the In shuttle is open, the model starts to analyze RHEED data in real-time. The model outputs are displayed as numerical values at the top of the interface and are converted to corresponding label characters on the right side. The growth status can be displayed in the “Reminder Information”. Before and after the QD formation, the “Reminder Information” will show up as “Stage 1” and “Stage 2”, respectively. It will display as “Finished” when the model results meet the targets several times after the QD formation.

ASSOCIATED CONTENT

Supporting Information

Details on RHEED characteristics of QDs with different labels, hardware wiring scheme for model deployment, program interface and deployment environment, the cropping area for RHEED images, details of the reference sample, the statistical analysis of the results of the “density model”. The video demonstrated QD growth experiments with “low” and “high” labels as targets, respectively. This material is available free of charge via the Internet at <http://pubs.acs.org>.

AUTHOR INFORMATION

Corresponding Author

*Email: zhaochao@semi.ac.cn

Author Contributions

C. S. and W. K. Z. contributed equally. C. Z. conceived of the idea, designed the investigations, and the growth experiments. C. S., W. K. Z. and M. Y. L performed the molecular beam epitaxial growth. C. S. and K. Y. X. did the sample characterization. C. S., C. Z., Z. Y. S, J. T., Z. F. W, and Z. M. W wrote the manuscript. C. Z. led the molecular beam epitaxy program. B. X. and Z. G. W. supervised the team. All authors have read, contributed to, and approved the final version of the manuscript.

Notes

The authors declare no competing financial interest.

ACKNOWLEDGMENT

This work was supported by the National Key R&D Program of China (Grant No. 2021YFB2206504), National Natural Science Foundation of China (Grant No. 62274159), the

“Strategic Priority Research Program” of the Chinese Academy of Sciences (Grant No. XDB43010102), and CAS Project for Young Scientists in Basic Research (Grant No. YSBR-056).

REFERENCES

- (1) Verma, A. K.; Bopp, F.; Finley, J. J.; Jonas, B.; Zrenner, A.; Reuter, D. Low areal densities of InAs quantum dots on GaAs(100) prepared by molecular beam epitaxy. *J. Journal of Crystal Growth.* **2022**, 592, 126715. DOI: 10.1016/j.jcrysGro.2022.126715
- (2) Jie, S.; Peng, J.; Zhan-Guo, W. Extremely low density InAs quantum dots realized in situ on (100) GaAs. *J. Nanotechnology.* **2004**, 15 (12), 1763. DOI: 10.1088/0957-4484/15/12/012
- (3) Chu, L.; Arzberger, M.; Böhm, G.; Abstreiter, G. Influence of growth conditions on the photoluminescence of self-assembled InAs/GaAs quantum dots. *J. Journal of Applied Physics.* **1999**, 85 (4), 2355-2362. DOI: 10.1063/1.369549
- (4) LeCun, Y.; Bengio, Y.; Hinton, G. Deep learning. *J. Nature.* **2015**, 521 (7553), 436-444. DOI: 10.1038/nature14539
- (5) Jordan, M. I.; Mitchell, T. M. Machine learning: Trends, perspectives, and prospects. *J. Science.* **2015**, 349 (6245), 255-260. DOI: 10.1126/science.aaa8415
- (6) Wakabayashi, Y. K.; Otsuka, T.; Krockenberger, Y.; Sawada, H.; Taniyasu, Y.; Yamamoto, H. Machine-learning-assisted thin-film growth: Bayesian optimization in molecular beam epitaxy of SrRuO₃ thin films. *J. APL Materials.* **2019**, 7 (10), 101114. DOI: 10.1063/1.5123019
- (7) Wakabayashi, Y. K.; Otsuka, T.; Krockenberger, Y.; Sawada, H.; Taniyasu, Y.; Yamamoto, H. Bayesian optimization with experimental failure for high-throughput materials growth. *J. npj Computational Materials.* **2022**, 8 (1), 180. DOI: 10.1038/s41524-022-00859-8

(8) Currie, K. R.; LeClair, S. R.; Patterson, O. D. Self-Directed, Self-Improving Control of a Molecular Beam Epitaxy Process. *J. IFAC Proceedings Volumes*. **1992**, *25* (28), 83-87. DOI: 10.1016/S1474-6670(17)49469-9

(9) Currie, K. R.; LeClair, S. R. Self-improving process control for molecular beam epitaxy. *J. The International Journal of Advanced Manufacturing Technology*. **1993**, *8* (4), 244-251. DOI: 10.1007/BF01748634

(10) Meng, Z.; Yang, Q.; Yip, P. C.; Eyink, K. G.; Taferner, W. T.; Igelnik, B. Combined use of computational intelligence and materials data for on-line monitoring and control of MBE experiments. *J. Engineering Applications of Artificial Intelligence*. **1998**, *11* (5), 587-595. DOI: 10.1016/s0952-1976(98)00024-4

(11) Uddin, G. M.; Ziemer, K. S.; Zeid, A.; Lee, Y.-T. T.; Kamarthi, S. Process control model for growth rate of molecular beam epitaxy of MgO (111) nanoscale thin films on 6H-SiC (0001) substrates. *J. The International Journal of Advanced Manufacturing Technology*. **2017**, *91* (1), 907-916. DOI: 10.1007/s00170-016-9674-1

(12) Kim, H. J.; Chong, M.; Rhee, T. G.; Khim, Y. G.; Jung, M.-H.; Kim, Y.-M.; Jeong, H. Y.; Choi, B. K.; Chang, Y. J. Machine-learning-assisted analysis of transition metal dichalcogenide thin-film growth. *J. Nano Convergence*. **2023**, *10* (1), 10. DOI: 10.1186/s40580-023-00359-5

(13) Liang, H.; Stanev, V.; Kusne, A. G.; Tsukahara, Y.; Ito, K.; Takahashi, R.; Lippmaa, M.; Takeuchi, I. Application of machine learning to reflection high-energy electron diffraction images for automated structural phase mapping. *J. Physical Review Materials*. **2022**, *6* (6), 063805. DOI: 10.1103/PhysRevMaterials.6.063805

(14) Kwoen, J.; Arakawa, Y. Classification of in situ reflection high energy electron diffraction images by principal component analysis. *J. Japanese Journal of Applied Physics.* **2021**, *60* (SB). DOI: 10.35848/1347-4065/abdad5

(15) Provence, S. R.; Thapa, S.; Paudel, R.; Truttmann, T. K.; Prakash, A.; Jalan, B.; Comes, R. B. Machine learning analysis of perovskite oxides grown by molecular beam epitaxy. *J. Physical Review Materials.* **2020**, *4* (8). DOI: 10.1103/PhysRevMaterials.4.083807

(16) Gliebe, K.; Sehirlioglu, A. Distinct thin film growth characteristics determined through comparative dimension reduction techniques. *J. Journal of Applied Physics.* **2021**, *130* (12), 125301. DOI: 10.1063/5.0059655

(17) Kwoen, J.; Arakawa, Y. Multiclass classification of reflection high-energy electron diffraction patterns using deep learning. *J. Journal of Crystal Growth.* **2022**, *593*, 126780. DOI: 10.1016/j.jcrysgro.2022.126780

(18) Lee, K. K.; Brown, T.; Dagnall, G.; Bicknell-Tassius, R.; Brown, A.; May, G. S. Using neural networks to construct models of the molecular beam epitaxy process. *J. IEEE Transactions on Semiconductor Manufacturing.* **2000**, *13* (1), 34-45. DOI: 10.1109/66.827338

(19) Zhang, L.; Shao, S. Image-based machine learning for materials science. *J. Journal of Applied Physics.* **2022**, *132* (10), 100701. DOI: 10.1063/5.0087381

(20) Vasudevan, R. K.; Tselev, A.; Baddorf, A. P.; Kalinin, S. V. Big-Data Reflection High Energy Electron Diffraction Analysis for Understanding Epitaxial Film Growth Processes. *J. ACS Nano.* **2014**, *8* (10), 10899-10908. DOI: 10.1021/nn504730n

(21) Xue, S.; Abhayaratne, C. Region-of-Interest Aware 3D ResNet for Classification of COVID-19 Chest Computerised Tomography Scans. *J. IEEE Access.* **2023**, *11*, 28856-28872. DOI: 10.1109/ACCESS.2023.3260632

(22) Nemcsics, Á.; Heyn, C.; Stemmann, A.; Schramm, A.; Welsch, H.; Hansen, W. The RHEED tracking of the droplet epitaxial grown quantum dot and ring structures. *J. Materials Science and Engineering: B.* **2009**, *165* (1), 118-121. DOI: 10.1016/j.mseb.2009.02.015

(23) Ozaki, N.; Takata, Y.; Ohkouchi, S.; Sugimoto, Y.; Ikeda, N.; Watanabe, Y.; Kitagawa, Y.; Mizutani, A.; Asakawa, K. Selective-Area Growth of Self-Assembled InAs-QDs by Metal Mask Method for Optical Integrated Circuit Applications. *J. MRS Online Proceedings Library.* **2011**, *959* (1), 1703. DOI: 10.1557/PROC-0959-M17-03

(24) Oikawa, S.; Makaino, A.; Sogabe, T.; Yamaguchi, K. Growth Process and Photoluminescence Properties of In-Plane Ultrahigh-Density InAs Quantum Dots on InAsSb/GaAs(001). *J. physica status solidi (b).* **2018**, *255* (4), 1700307. DOI: 10.1002/pssb.201700307

(25) Yamaguchi, K.; Kanto, T. Self-assembled InAs quantum dots on GaSb/GaAs(001) layers by molecular beam epitaxy. *J. Journal of Crystal Growth.* **2005**, *275* (1), e2269-e2273. DOI: 10.1016/j.jcrysgro.2004.11.363

(26) Chen, Y. H.; Krishna, T.; Emer, J. S.; Sze, V. Eyeriss: An Energy-Efficient Reconfigurable Accelerator for Deep Convolutional Neural Networks. *J. IEEE Journal of Solid-State Circuits.* **2017**, *52* (1), 127-138. DOI: 10.1109/JSSC.2016.2616357

(27) Jiang, J.; Feng, X.; Liu, F.; Xu, Y.; Huang, H. Multi-Spectral RGB-NIR Image Classification Using Double-Channel CNN. *J. IEEE Access.* **2019**, *7*, 20607-20613. DOI: 10.1109/ACCESS.2019.2896128

(28) Xu, W.; Gao, F.; Zhang, J.; Tao, X.; Alkhateeb, A. Deep Learning Based Channel Covariance Matrix Estimation With User Location and Scene Images. *J. IEEE Transactions on Communications.* **2021**, *69* (12), 8145-8158. DOI: 10.1109/TCOMM.2021.3107947

(29) Codella, N. C. F.; Nguyen, Q. B.; Pankanti, S.; Gutman, D. A.; Helba, B.; Halpern, A. C.; Smith, J. R. Deep learning ensembles for melanoma recognition in dermoscopy images. *J. IBM Journal of Research and Development*. **2017**, *61* (4/5), 5:1-5:15. DOI: 10.1147/JRD.2017.2708299

(30) Komiske, P. T.; Metodiev, E. M.; Schwartz, M. D. Deep learning in color: towards automated quark/gluon jet discrimination. *J. Journal of High Energy Physics*. **2017**, *2017* (1), 110. DOI: 10.1007/JHEP01(2017)110

(31) Reith, F.; Koran, M. E.; Davidzon, G.; Zaharchuk, G. Application of Deep Learning to Predict Standardized Uptake Value Ratio and Amyloid Status on ^{18}F -Florbetapir PET Using ADNI Data. *J. American Journal of Neuroradiology*. **2020**, *41* (6), 980-986. DOI: 10.3174/ajnr.A6573 %J American Journal of Neuroradiology

(32) Qassim, H.; Feinzimer, D.; Verma, A. Residual squeeze vgg16. *J. arXiv*. **2017**. DOI: 10.48550/arXiv.1705.03004

(33) Li, B.; He, Y. An Improved ResNet Based on the Adjustable Shortcut Connections. *J. IEEE Access*. **2018**, *6*, 18967-18974. DOI: 10.1109/ACCESS.2018.2814605

(34) Aziz, L.; Salam, M. S. B. H.; Sheikh, U. U.; Ayub, S. J. I. A. Exploring deep learning-based architecture, strategies, applications and current trends in generic object detection: A comprehensive review. *J. IEEE Access*. **2020**, *8*, 170461-170495. DOI: 10.1109/ACCESS.2020.3021508

(35) Wu, X.; Ji, Q. J. A. TBRNet: two-stream BiLSTM residual network for video action recognition. *J. Algorithms*. **2020**, *13* (7), 169. DOI: 10.3390/a13070169

(36) Khanna, A.; Londhe, N. D.; Gupta, S.; Semwal, A. A deep Residual U-Net convolutional neural network for automated lung segmentation in computed tomography images. *J.*

Biocybernetics and Biomedical Engineering. **2020**, *40* (3), 1314-1327. DOI: 10.1016/j.bbe.2020.07.007

(37) Liao, Y.; Xiong, P.; Min, W.; Min, W.; Lu, J. Dynamic Sign Language Recognition Based on Video Sequence With BLSTM-3D Residual Networks. *J. IEEE Access*. **2019**, *7*, 38044-38054. DOI: 10.1109/ACCESS.2019.2904749

(38) Xue, F.; Ji, H.; Zhang, W. Mutual information guided 3D ResNet for self-supervised video representation learning. *J. IET Image Processing*. **2020**, *14* (13), 3066-3075. DOI: 10.1049/iet-ipr.2020.0019

(39) Liu, W.; Wu, G.; Ren, F.; Kang, X. DFF-ResNet: An insect pest recognition model based on residual networks. *J. Big Data Mining and Analytics*. **2020**, *3* (4), 300-310. DOI: 10.26599/BDMA.2020.9020021

(40) Fakhry, A.; Zeng, T.; Ji, S. Residual Deconvolutional Networks for Brain Electron Microscopy Image Segmentation. *J. IEEE Transactions on Medical Imaging*. **2017**, *36* (2), 447-456. DOI: 10.1109/TMI.2016.2613019

(41) Ganokratanaa, T.; Aramvith, S.; Sebe, N. Video anomaly detection using deep residual-spatiotemporal translation network. *J. Pattern Recognition Letters*. **2022**, *155*, 143-150. DOI: 10.1016/j.patrec.2021.11.001

(42) Zhang, K.; Sun, M.; Han, T. X.; Yuan, X.; Guo, L.; Liu, T. Residual Networks of Residual Networks: Multilevel Residual Networks. *J. IEEE Transactions on Circuits and Systems for Video Technology*. **2018**, *28* (6), 1303-1314. DOI: 10.1109/TCSVT.2017.2654543

(43) Yu, H.; Liu, J.; Chen, C.; Heidari, A. A.; Zhang, Q.; Chen, H. Optimized deep residual network system for diagnosing tomato pests. *J. Computers and Electronics in Agriculture*. **2022**, *195*, 106805. DOI: 10.1016/j.compag.2022.106805

(44) Zhu, Z.; Zhai, W.; Liu, H.; Geng, J.; Zhou, M.; Ji, C.; Jia, G. Juggler-ResNet: A Flexible and High-Speed ResNet Optimization Method for Intrusion Detection System in Software-Defined Industrial Networks. *J. IEEE Transactions on Industrial Informatics.* **2022**, *18* (6), 4224-4233. DOI: 10.1109/TII.2021.3121783

(45) Cheng, Y.; Wang, D.; Zhou, P.; Zhang, T. J. a. p. a. A survey of model compression and acceleration for deep neural networks. *J. arxiv.* **2017**. DOI: 10.48550/arXiv.1710.09282

(46) Sutton, R. S. Learning to predict by the methods of temporal differences. *J. Machine Learning.* **1988**, *3* (1), 9-44. DOI: 10.1007/BF00115009

(47) Vamathevan, J.; Clark, D.; Czodrowski, P.; Dunham, I.; Ferran, E.; Lee, G.; Li, B.; Madabhushi, A.; Shah, P.; Spitzer, M.; et al. Applications of machine learning in drug discovery and development. *J. Nature Reviews Drug Discovery.* **2019**, *18* (6), 463-477. DOI: 10.1038/s41573-019-0024-5

(48) Joyce, T. B.; Bullough, T. J. Beam equivalent pressure measurements in chemical beam epitaxy. *J. Journal of Crystal Growth.* **1993**, *127* (1), 265-269. DOI: 10.1016/0022-0248(93)90619-8

(49) Sfaxi, L.; Bouzaiene, L.; Sghaier, H.; Maaref, H. Effect of growth temperature on InAs wetting layer grown on (113)A GaAs by molecular beam epitaxy. *J. Journal of Crystal Growth.* **2006**, *293* (2), 330-334. DOI: 10.1016/j.jcrysgr.2006.05.042

(50) Song, H. Z.; Usuki, T.; Nakata, Y.; Yokoyama, N.; Sasakura, H.; Muto, S. Formation of InAs quantum dots from a subcritical InAs wetting layer: A reflection high-energy electron diffraction and theoretical study. *J. Physical Review B.* **2006**, *73* (11), 115327. DOI: 10.1103/PhysRevB.73.115327

(51) Guo, S. P.; Ohno, H.; Shen, A.; Matsukura, F.; Ohno, Y. InAs self-organized quantum dashes grown on GaAs (211)B. *J. Applied Physics Letters*. **1997**, *70* (20), 2738-2740. DOI: 10.1063/1.119007

(52) Okumura, S.; Fujisawa, K.; Naruke, T.; Nishi, K.; Onishi, Y.; Takemasa, K.; Sugawara, M.; Sugiyama, M. Impact of low-temperature cover layer growth of InAs/GaAs quantum dots on their optical properties. *J. Japanese Journal of Applied Physics*. **2022**, *61* (8), 085503. DOI: 10.35848/1347-4065/ac7caa

(53) Lee, S.; Lazarenkova, O. L.; von Allmen, P.; Oyafuso, F.; Klimeck, G. Effect of wetting layers on the strain and electronic structure of InAs self-assembled quantum dots. *J. Physical Review B*. **2004**, *70* (12), 125307. DOI: 10.1103/PhysRevB.70.125307

(54) Offermans, P.; Koenraad, P. M.; Nötzel, R.; Wolter, J. H.; Pierz, K. Formation of InAs wetting layers studied by cross-sectional scanning tunneling microscopy. *J. Applied Physics Letters*. **2005**, *87* (11), 111903. DOI: 10.1063/1.2042543

(55) Ruiz-Marín, N.; Reyes, D. F.; Stanojević, L.; Ben, T.; Braza, V.; Gallego-Carro, A.; Bárcena-González, G.; Ulloa, J. M.; González, D. Effect of the AlAs capping layer thickness on the structure of InAs/GaAs QD. *J. Applied Surface Science*. **2022**, *573*, 151572. DOI: 10.1016/j.apsusc.2021.151572

(56) He, K.; Zhang, X.; Ren, S.; Sun, J. Identity Mappings in Deep Residual Networks. In *Computer Vision – ECCV 2016*, Cham, October 11-14, 2016, 2016; Leibe, B., Matas, J., Sebe, N., Welling, M., Eds.; Springer International Publishing: Switzerland, 2016; pp 630-645. DOI: 10.1007/978-3-319-46493-0_38.

(57) LeCun, Y.; Boser, B.; Denker, J. S.; Henderson, D.; Howard, R. E.; Hubbard, W.; Jackel, L. D. J. N. c. Backpropagation applied to handwritten zip code recognition. *J.* **1989**, *1* (4), 541-551. DOI: 10.1162/neco.1989.1.4.541

Table of Contents Graphic

